Settle3D - A numerical generator for artificial porous media

G. Blöcher* & G. Zimmermann

*GeoForschungsZentrum Potsdam, Telegrafenberg, D-14473 Potsdam
(*Corresponding author. Phone: +49 331 288 1414, E-mail:
bloech@gfz-potsdam.de)*

Abstract

Reservoir rocks, regardless of what kind (oil-, gas- or water-bearing), are classified by their specific properties. Most rock properties, such as storage, permeability, electric conductivity, heat capacity and so on are determined by laboratory experiments and field tests under different external conditions. Besides temperature, pressure and chemical reactions, also the geometry of the pore space as well as porosity control the specific behaviour of a rock. In most experiments, heterogeneous deformation of the pore space, changes in porosity and inner surface or closing of micro-cracks or pore-throats, cannot be observed directly. To study the dynamic processes behind these changes, we developed the sedimentary tool "Settle3D". With this software it is possible to generate different clastic rocks in a discrete way, which means that each grain inside this rock can be handled separately. The resulting porous medium can be directly used as import structure for different mechanical, hydraulic and thermal simulations. So the structural information of rocks can be linked to the petrophysical behaviour of porous media. To address these questions, we will present the development as well as the possibilities of "Settle3D". These include the generation of various 3D grainpacks, handling of input parameters (such as grain size distribution of different materials), sedimentary processes via direct collision procedures and an analysis of the final pore space geometry.

Key words: artificial porous media, pore models

1 Introduction.

The traditional approach to modelling the hydraulic and petrophysical behaviour of porous media (such as deformation or fluid transport) is to approximate the sediment structure as a continuous medium (Bachmat and Bear, 1986). This procedure can be inproved by using a double or multi continuum

model for representing fractured porous media (Balhoff et al., 2007; Wu et al., 2001) or karst aquifers [1] (Lang, 1995). With the restriction that the modelled dimension is a representative elementary volume REV (Bear, 1972; Guéguen et al., 1998), this approach can satisfy many applications. This means that the model area is large compared to the individual pore.

The parameterisation of such models is often based on laboratory or field experiments and the determined characteristics are assumed as similar for any material. Some phenomena such as a change in permeability, electrical conductivity or Skempton coefficient, all depending on applied effective stress, can be measured by laboratory experiments but cannot be completely explained by the models described above. For the reason that the direct influence of microscopic pore space change on the macroscopic behaviour is technically limited, a number of pore models have been developed [2] (a review is given in Valvatne and Blunt, 2004). The basic approach in these models differs: Including stochastic distributed grains (Adler et al., 2002; Manwart et al., 2000; Thovert et al., 2001) and capillary networks (Adler et al., 1992), fractals (Adler, 1988; Spangenberg, 2005), packed grains (Matthews et al., 1996) and others. However, all of them have the same goal: The generation of an artificial porous media which can represent natural rocks.

The resulting pore model can be processed by different types of simulation software, which can help to predict what happens when the pore geometry changes. The driving forces for a change in geometry are hydraulic, thermal, mechanical or chemical processes and by means of the pore model these processes can be linked.

In order to produce an adequate approximation of porous media, we simulate the fundamentals of the sedimentation process at the single grain scale. In this paper we will show the way from the primordial grain up to completely artificial porous media, with special focus on sedimentation process of sandstones. The sedimentation procedure itself is not limited and can simulate sedimentary processes of any rock type.

---

[1] U. Mohrlok, 1996. Parameter-Identifikation in Doppel-Kontinuum-Modellen am Beispiel von Karstaquiferen (Parameter identification in double continuum models by example of karst aquifers). Tübinger Geowissenschaftliche Arbeiten, Institut und Museum für Geologie und Paläontologie der Universität Tübingen, Tübingen, Germany.
http://w210.ub.uni-tuebingen.de/dbt/volltexte/2005/2130/

[2] G. W. Horgan, 1996. A review of soil pore models. Biomathematics and Statistics Scotland, James Clerk Maxwell Building, King's Buildings, Edinburgh, Scotland.
http://citeseer.ist.psu.edu/horgan96review.html

2   The primordial grain.

The first step in modelling a complete sedimentary rock structure is to define a primordial grain. This grain should fulfil the requirements of a real grain such as a variation in shape and size, a definition of surface roughness and the re- alisation of a detailed body structure. Besides these geometrical specifications the handling of the artificial grain via different computer routines should be as simple as possible. We found that the basic shape of an icosahedron (Fig. 1) can satisfy the geometrical and technical requirements best and can be easily converted into a FE-mesh. A regular icosahedron is one of the five platonic solids. It is a convex regular polyhedron having 20 equilateral triangles as faces, with five connected at each of the twelve nodes. It has 30 edges with length a, which can be calculated by the radius r of the circumscribed sphere:

$$a = \frac{4r}{\sqrt{10 + 2\sqrt{5}}}. \tag{1}$$

The surface area A and the volume V of a regular icosahedron of edge length a are:

$$A = 5\sqrt{3}a^2, \tag{2}$$

$$V = \frac{5}{12}(3 + \sqrt{5})a^3. \tag{3}$$

An icosahedron can be considered as a rough approximation for a sphere. Based on this geometry it was possible to design different types of grains. Besides the change in size and the increase in accuracy by subdivision of the faces also a morphing of the surface and application of surface roughness are possible. Therefore, the initial icosahedron geometry can be changed and modified in such a way that it results in a real grain-like structure.

3   Refinement.

There is a simple way to increase the accuracy of grain approximation by sub- dividing the faces of the icosahedron. Imagine the icosahedron is surrounded by a sphere and subdivide the triangles by dividing the edges in the middle. The newly inserted nodes lie slightly inside the sphere, so they are pushed to the surface by multiplying the normalised node with the radius. By this subdivision process each triangle is divided into four new triangles. Due to the surface lifting of the nodes the inner triangle is slightly bigger than the three

triangles on the former edges. The refinement procedure can be repeated for arbitrary accuracy as shown in Figure 2.

With each refinement the resulting structure becomes more and more sphere-like, but the number of nodes, edges and triangles is increasing exponentially (Tab. 1) and should not exceed an acceptable level with respect to the computer performance. The number of nodes N, edges E and faces F can be calculated at each refinement level n by means of the following equations:

$$N = 10 \times 4^n + 2, \tag{4}$$

$$E = 30 \times 4^n, \tag{5}$$

$$F = 20 \times 4^n. \tag{6}$$

4 Grain morphology.

The three principal aspects which define a grain are the shape, sphericity and roundness (Tucker, 1991). The shape can be coarsely classified by ratios of the long, intermediate and small axes of the grain and results in four types, which are oblate (tabular or disc-shaped), equant (cubic or spherical), bladed and prolate (rod-shaped). Sphericity describes how closely a grain shape reaches a sphere and roundness qualifies the curvature of the edges of the grain. Six classes from "very angular" to "well rounded" are usually introduced to describe the roundness of a grain. In order to obtain an exact expression for sphericity as well as for roundness different formulas were developed (Dobkins and Folk, 1970).

Inside "Settle3D" the variation in morphology is realised by changing the position of the body-defining nodes. The possibilities of morphing the structure are unlimited, grains can be stretched or compressed, nodes above or below a defined border can be reset to a limit and also an additional noise or an explicit function can change the surface structure of the grain. At the current state the grain shaping is directly implemented in the source code and the user can switch the predefined types by changing the input parameters (see section 6). Some of the predefined types and their variation are shown in Figure 3, but they give only a first impression of the program potential. The ratio of the principal axes for the actually implemented types representing quartz, feldspar and clay has been obtained from thin section micrographs of different sources (Scholle, 1979; Adams et al., 1986).

4

5 Structure of the model.

One of the most important issues for developing such complex microstructures of sedimentary rocks is to classify the participating geometries accurately. The smallest unit of a grain is one node in a three dimensional volume and is therefore given by its three coordinates x, y and z. As described in the section 2 the grain is composed of a defined amount of triangles, which themselves are defined by three nodes at their edges. To avoid a double declaration of nodes, the triangles only point to the node definitions and don't declare new nodes. According to the refinement level, each grain is constructed of a specific amount of triangles and nodes, defining the outer surface of the grain. In addition to this surface geometry the location of the centre of gravity (CG) and up to three contact points with other grains specify the grain. Each grain of the model is placed into a predefined finite volume depending on the location of its CG. The complete model volume is the sum of all these finite volumes.

Besides the geometric data each of the substructures can also store various properties as well as functions to handle this kind of structure. In addition to the node definition, the normal vector for each triangle is calculated as well. Its benefit will be explained in the section 7. For a grain the scalar properties volume, surface area, density, shape type, maximum diameter and colour are implemented. Further the movement functions translation and rotation, splitting-up to the three components x, y and z and a draw- and some export routines are located inside the grain environment. In order to get more evidence of the grain situation, feedbacks from geometric stability, the slope of the contact surface and the position related to the model borders are included. The geometric stability is given by the fact, that a grain is stable, if the vertical projection of the CG is inside the vertical projection of at least three contact points. It is unstable, if the CG is outside of the contact point polygon or the slope of the contact surface is higher then a defined friction angle. The grain is out of further calculation, if its surface touches the preset model borders. The finite model volumes just store the grains which have settled down. A complete view of the model structure including some of the functions and properties of the substructures is shown in Figure 4.

6 Input parameters (model data).

The previously described dynamic structure of the model can be adjusted by user-defined parameters. These parameters affect the structure data from the smallest node to the entire volume. All input parameters can be given as an input file or can directly be entered within the software environment. They include the model dimension, the maximum amount of grains, the refinement

level, the grain densities, the grain-size scale and the friction angle.

At the current state, the dimension of the model is given by x, y and z values, where x and z are the horizontal dimensions and y the vertical dimension. "Settle3D" subdivides the entire volume to cube shaped finite volumes, which can store the settled grains. The maximum amount of grains as well as the refinement level for each grain can also be changed. This affects the total number of nodes and triangles that have to be handled by the model procedures.

In "Settle3d" three predefined grain shapes exist: quartz (spherical), feldspar (cubical) and mica (flat cuboid). Further grain shapes as well as surface structures of the grains have to be implemented in the future. For generating the grain shape and the grain size, the parameters density and grain distribution are used. The grain distribution is implemented as a grain mass spectrum. This means that for each grain type (quartz, feldspar and mica) the cumulative mass percentage depending on the grain size fraction must be given, where the mass percentage corresponds to the total mass of all grain types and sizes. By means of density, which is defined for each grain type, the tool will generate a grain of the right shape and size satisfying the given distribution. There, the shape is fixed by the given grain mass fraction and the size is selected randomly for each grain size fraction. Each user-specific distribution for all grain types including bimodal and higher order distributions can be generated. At the moment each generated grain is dropped vertical from the top into the model area.

Scaling the grain size is not straight forward (Füchtbauer, 1988, and references therein): We used a simple and standard classification according to "Deutsches Institut für Normung" (DIN4022). The common parameter friction angle indicates whether a settled grain is sliding or is stable on is current position.

7   Sedimentary process.

Mechanical particle movements are sub-classified into suspension, saltation and traction (Selley, 2000; Reineck and Singh, 1980, and references therein). During the suspension process the particles are carried within the fluid and never touch the ground. Movement of grains downward with subsequent upward trajectories and a further gentle downward path are known as bouncing or saltation process. If the grains remain in contact with the ground and are moving by rolling or sliding, it is called traction. In sedimentary processes, the final movement of grains is rolling or sliding on pre-deposited grains. Therefore, we excluded the transportation processes suspension and saltation in "Settle3D". The remaining traction process can be reduced to a combination of rotation and translation of the grains. During these rotation and translation

movements, the subjected grain collides and intersects with other grains. The calculation of the contact points depending on the trajectories is one of the main tasks of "Settle3D". Inside 3D computer games or 3D computer graphics the detection of collision between two or more virtual object is one of the great challenges. Often it will be tested, whether a collision occurred or not; and it will be decided what happened next after a collision [3] (Mezger et al., 2002). In the most cases the detection of collision is based on a triangle intersection test [4] (Möller, 1997), because most computer geometries are generated of triangles. With "Settle3D" all possible contacts are determined explicitly and the grains are moved by the shortest distance calculated. Therefore no triangle intersection test or collision detection is necessary. The direct calculation of the contacts via translation or rotation and its requirements will be described in the following sections in more detail.

8 Preselection of potential collision triangles.

To minimize the necessary processor time for calculating the intersections, a pre-selection of potential collision triangles is performed first. The preselection process is started at a coarse level with a stepwise refinement. A total of four steps for translation and rotation are performed. For both movements the preselection is starting at model dimension and finally ends at the triangle dimension. In Figure 5 the stepwise refinement of the selection for calculating the vertical translation is shown.

8.1 Preselection for translation processes.

The first step of refinement is a selection of all settled grains which are located inside a specific radius around the CG of the falling grain in the x and z directions. Therefore the volume of interest describes a cylinder with a radius of the maximum possible grain size and a length of the vertical dimension of the model. In the second step all grains are chosen which intersect with the pathway of the falling grain. The next delimitation takes place at the triangle size, where only triangles can intersect which are directed face to face. These can be determined by using the normal vectors of the triangles. For the final calculation only triangles inside the pathways of each preselected triangle of the falling grain are used.

---

[3] K. Fauerby, 2003. Improved collision detection and response.
http://www.peroxide.dk/papers/collision/collision.pdf

[4] O. Devillers and P. Guigue, 2002. Faster triangle-triangle intersection tests. Internal Report 4488, INRIA. http://hal.archives-ouvertes.fr/docs/00/07/21/00/PDF/RR-4488.pdf

8.2 Preselection for rotation processes.

For the rotation process the preselection is similar to the translation process and the first step for both selections is identical (Fig. 6). The second step includes all grains, which are inside or interfere with the surrounding sphere given by the CG and the grain size taken as center and radius, respectively. The third step selects all triangles of the rotating grain which are orientated in the rotation direction and all triangles of the settled grains which are diametrically oriented to the rotation of the falling grain. There, the orientations are given by the normal vectors. The last preselection step reduces the amount of triangles by excluding all triangles of the falling grains which are outside of the disc like volume which arises from rotating the preselected triangles of the falling grain around its pivot point.

9 Collision routines.

The now preselected triangles of the falling grain regardless of its specific movement can collide with the preselected triangles of the settled grains in different ways. The most obvious way is that one single node hits the face of another triangle, but also a line-line intersection is possible (Fig. 7).

All in all, fifteen collisions subdivided into six point-triangle and nine line-line intersections for only two triangles are possible. So each node of the moving triangle can hit the face of the stationary triangle and vice versa and each line of the moving triangle can interfere with each line of the stationary triangle. But the calculation of the intersection points depends on the kind of movement that the selected triangle performs. Therefore, we have to develop for translation as well as for rotation point-triangle and line-line intersection routines. A detailed description of the required procedures is provided in Appendix A.

10 Post-selection of the calculated intersection points.

With the previously specified collision routines a large number of intersection points are calculated for one single movement step. To find the right intersection point, which results from a projection of the original to the image point, we have to make several decisions: For the translation process the intersection point with the shortest distance between original and image is taken. In contrast to translation, not all calculated intersection points of rotation are potential collision points. The reason for this is that some sub-areas of the

preselected triangles cannot hit another triangle. The trajectories of these sub-areas are in the shadow of the rotating edges. Figure 8 illustrates a simplified case study of this problem where the investigation is reduced to 2D.

The question is: Which part of the given lines can possibly hit another line. It follows that only the sub-lines which rotate away in terms of the grain can collide with other objects. In order to determine these parts the base point of the pivot point on each line is calculated. With regard to these base points only the sinistral orientated sub-lines rotate away for a clockwise rotation. Carried forward to 3D, we have to project the rotation axis vertically into a triangle plane. Consequently, only the sub-area on the left side of this projection can intersect with other grains. Therefore, only the intersection points which are members of these sub-areas can be taken as potential collision points. From all these intersection points the one with the smallest related rotation angle is selected for the rotation step.

11 Pathway of a falling grain.

Inside "Settle3D" the sedimentary process is rebuilt by dropping grains successively at a randomly selected xy-position nto the model area. After dropping, each grain must pass the same movement sequences. The sequences start with a vertical translation of the grain until it collides with another grain or touches the bottom of the model. The calculated intersection or touching point becomes the first contact point of the grain. If this contact point is not a collision point, then the grain is classified as settled and the sequence is restarted with the next grain. In case of a collision the sequence will continue with the rotation process. To keep the rotation as simple as possible we reduce the degree of freedom by transforming the basis of the preselected grains (Eq. 7):

$$\overrightarrow{N'} = (\overrightarrow{N} - \overrightarrow{T}) \times R_y \times R_z \times R_y^{-1} + \overrightarrow{T}. \tag{7}$$

Here, all nodes $\overrightarrow{N}$ of the preselected grains are shifted by $\overrightarrow{T}$, so that the first contact point is translated into the origin. By means of the CG coordinates each node is rotated around the y-axis afterwards, so that the CG is located inside the xy-plane and the related z-coordinate is zero. After these transformations only a clockwise rotation R_z around the z-axis has to be calculated. This rotation leads to the identification of the second contact point, which together with the first one builds the new rotation axis. Now the inversion of the transformations takes place and "Settle3D" determines whether the falling grain is rotated out of the model-area and a new grain is generated or the next rotation step can be calculated. In that case and for each following rotation we transform the origin to reduce the of degree of freedom as shown in Equation

8:

$$\overrightarrow{N'} = (\overrightarrow{N} - \overrightarrow{T}) \times R_y \times R_x \times R_z \times R_x^{-1} \times R_y^{-1} + \overrightarrow{T}. \tag{8}$$

This transformation moves the two contact points into the z-axis and the CG into the xy0-plane. The required transformation vector $\overrightarrow{T}$ as well as the two rotation matrices R_x and R_y are calculated by means of the two contact points. After the second rotation step a third contact point will be determined. The two alternatives are: The grain is in a stable position or it keeps on moving. For this purpose a stability-check function is implemented that can identify the next movement depending on the relative position between the CG and the three contact points (Fig. 9). If the vertical projection of the CG into the triangle plane defined by the three contact points is located inside the limits of the triangle, then the grain is stable or can fall again. It falls again, if none of the contact points bear on another triangle face. If this is not the case, the grain is stable and "Settle3D" will continue with the next grain. If the vertical projection of the CG is outside the contact point triangle, then a next case differentiation takes place. We have to distinguish whether the CG is located above or below the triangle plane. In both cases one of the three contact points will lose contact and a further rotation around the line given by the two remaining contact points will occur. For this purpose, also the bisecting lines of the contact point triangle are required, as shown in Figure 9.

In the case that the falling grain is classified as stable, a further check of a possible sliding movement takes place. If the user defined friction angle is smaller than the angle between the contact point triangle and a horizontal plane, then the grain will be completely removed from the model. This removal does not affect the model statistics, because it occurs infrequently and the empty spot will be replaced by another grain. In the other case the grain remains inside the model and will be added to the settled grains. A grain will also be added to the model if one of its movements results in an intersection with the model boundaries.

Recapitulating all the single movements, the trajectory of the grain is described by an alternation between translation and rotation, both of them satisfying the physical laws.

12   The models.

By means of the described routines we are able to simulate the sedimentation of complete sedimentary rock samples. To show the variation of possibilities

ten different sediment structures have been generated. In order to keep these models comparable, the input data of all models are similar. The size of each model is $3mm \times 3mm \times 3mm = 27mm^3$ and the detail level of the grains is two, which correlates with a 1st order refinement. Therefore, only the variation of grain types, the grain size distribution and the combination of the sedimentary routines remain to affect the microstructure of the virtual sandstone. The three momentarily available types are sphere like quartz, cubic feldspar and flat clay. We started with a simple model, only containing quartz and added successively feldspar and clay for the following simulations.

Besides the grain type combination, the variation of sorting and the resulting change in microstructure were tested. For this purpose we increased the range of grain size from one (medium sand) up to three (coarse silt - medium sand) fractions. Furthermore, for each grain size distribution we calculated the Trask sorting coefficient So defined by the following equation (Trask, 1932):

$$So = \frac{P_{75}}{P_{25}}, \tag{9}$$

where P_n is the grain size in millimetres at the nth percentage frequency. According to this definition a sandpack with grains of the same size has a sorting coefficient of one. For a medium size sand the grain size ranges from 0.2 to 0.63mm and the correlating sorting coefficient is $So = 1.1$. For the next more poorly sorted sandstone containing 20% fine sand and 80% medium sand the sorting coefficient is $So = 1.8$ and finally a poorly sorted sandstone composed by 5% coarse silt, 25% fine sand and 70% medium sand has a Trask sorting coefficient of approximately $So = 3.0$.

At last we investigated the model dependency of the implemented sedimentation routines on the sedimentary microstructure. The test started with the sedimentation of artificial sandstone by using only the translation routine. This means that a falling grain is added to the sandstone if it collides the first time with the settled grains and no rotation or sliding takes place. In a second model run we enhanced the sedimentation process by adding the rotation routine. Hence, a combination of translation and rotation leads to the more dense sedimentation structure. To investigate the sliding algorithm and the impact of it, the remaining sliding routine was added in a third step. The above described variations in grain type, grain size and sedimentation routines lead to $3^3 = 27$ potential combinations. In Figure 10 ten of them are shown.

11

12.1 Results of the models.

Two important aspects of sedimentary rocks are their porosity and permeability. Porosity is a measure of the pore space. Two porosity types can be defined: the absolute porosity P_t including the complete pore space and the effective porosity P_e including the interconnected pore space with free water. For water-filled sandstone the effective porosity does not include the immobile water bound to the grain-pore interface. The thickness of the bound-water films varies depending on the mineral content, the water chemistry, and should not exceed 0.5 microns (Polubarinova-Kocina, 1962): A water film thickness of 0.4 microns is assumed for the following calculations. Therefore, the porosities can be calculated by means of the following equations:

$$P_t = \frac{bulk\ volume - grain\ volume}{bulk\ volume}, \tag{10}$$

$$P_e = \frac{bulk\ volume - (grain\ volume + bound\ volume)}{bulk\ volume}. \tag{11}$$

The bound volume (Eq. 11) is defined by the inner grain surface and the thickness of the bound water film:

$$bound\ volume = inner\ surface \times 0.4\mu m. \tag{12}$$

Besides the effective porosity the pore space geometry including size, shape and connectivity and the fluid properties affect the permeability of the sandstone. But the investigation of geometry-permeability relationships goes beyond the scope of this work. Therefore, the above mentioned porosities, inner surface and the amount of grains as well as grain volume were taken into account to obtain a primary analysis of the generated sandstones. All determined values are listed in Table 2.

The interpretation of the model results is separated into technical and geological aspects. On the technical side it is obvious that the largest change in microstructure occurs by implementing the rotation routine to the models. In contrast, an additional combination with the sliding routines does not have a large effect. From the geological point of view the following general relations between porosity, sorting and grain size distribution for siliciclastic sediments must be satisfied:

- poorer sorting results in lower porosity (Schopper, 1982)
- smaller grain size which corresponds to different grain types results in larger porosity (Buckingham, 2001)

12

- smaller grain size results in greater bound water volume (Davis and Wiest, 1966).

Packing or consolidation of grains can change porosity and permeability (Tucker, 1991) as well. Here, the packing also depends on the size, shape and sorting of the grains. Due to the fact that only point contacts are realized by "Settle3D" and no concavo-convex or sutured contacts can occur these aspects are not investigated in what follows.

For the first (sorting-porosity) relation the results of the single grain type models including translation and rotation were compared. There the Trask sorting coefficient increases from 1.1 for a single fraction well-sorted sandstone to 3.0 for the poorly-sorted sandstone with three grain fractions. Simultaneously, the porosity decreases from 51.62% over 46.68% to 43.53% and therefore validates the assumed relation.

The second (size-porosity) relation does not exist where size alone is varied. Porosity is dimensionless and it is scale invariant. Since for many geologic materials grain size and shape correlate then increasing finer grain size material is correlated with porosity. Therefore, for the second (size-porosity) relation the models including different types but only one grain fraction were analysed. For these models a combination of translation, rotation and sliding was used. Although all of these models have one single grain fraction, the volume of the grains is different. Due to the fact that the cubic and the flat grains have a smaller volume for the same diameter than the sphere like grains, more grains are necessary to fill the model area. Hence, the amount of required grains increases from 375 for the quartz model to 739 grains for the model containing a combination of flat, cubic and spherical grains. This indicates that the size of the grains must decrease from the first to the third model. At the same time the porosity is increasing from 50.05% over 55.65% to 59.80% and therefore fulfils the second relation. Besides the smaller grain size another aspect affects the porosity: the flat and cubic grains can cover free pore spaces and make these inaccessible for adjacent grains.

For the third (effective porosity-size) relation the same models as for the sorting-porosity relation were analysed. Here, the absolute porosity decreases by 8.09% from 51.62% to 43.53% and the effective porosity by 8.51% from 51.36 to 42.85%. This results from an increase of the inner surface, which corresponds to an increase of adhesive water volume. Consequently, all relations can be reproduced by the sedimentation software "Settle3D".

12.2   Comparison of 2D and 3D geometry.

Besides computer tomography (CT) and scanning electron microscopy (SEM) for three dimensional studies, the digital image analysis is a well established procedure to classify the pore space geometry of porous media in 2D. This direct method quantifies information about pore size, pore shape and pore distribution (Trautwein, 2005) as well as grain parameters obtained from thin section micrographs. An extrapolation of the resulting geometrical parameters into a 3D pore space characteristics is based on the methods of stereology (Underwood, 1970). The basic principle is that inside an isometric microstructure the portion of volume of one structure corresponds to the area-, linear- and the point-data of the thin section micrograph. A proof is shown in Appendix B.

For the generated microstructure of "Settle3D" the three dimensional microstructure of the generated sandstone is known. By means of cutting planes along the three principal axes it is possible to prove the conclusions based on stereology. For this purpose we created virtual thin section micrographs for each model by cutting the complete structure at 50% of the x, y and z dimension as shown in Figure 11.

In the cross-section images we separated pore space, grains and the pore-grain interface. For the reason that the interface area cannot clearly be allocated to pore space or grain area we excluded this area from further analyses. After this optimization we determined the 2D porosity for each cross section and compared the results with the 3D data as shown in Table 3. It is obvious that the x, y and z oriented porosities for each model are in the same range. This indicates an isometric microstructure in 3D. Furthermore, the average of the three directional components matches the 3D porosity and we can conclude that the 2D pore structure of thin-section micrographs represents the 3D geometry.

13   Meshing.

For the later use as a geometrical input-structure for a coupled process simulation it is necessary to convert the surface related geometry of "Settle3D" into a real 3D geometry. For this purpose the tetrahedrisation software TetGen[5] is used. Due to the fact that the grains in "Settle3D" only intersect in single

---

[5]   H. Si, 2007. TetGen: A quality tetrahedral mesh generator and three-dimensional Delaunay triangulator. Research Group of Numerical Mathematics and Scientific Computing, Weierstrass Institute for Applied Analysis and Stochastics, Berlin, Germany.
http://tetgen.berlios.de

points, a tetrahedrisation can cause numerically unstable elements. Therefore a preprocessing clean up of the generated structure has to be performed. The clean up process deletes nodes with identical coordinates and merges nodes which are close together. Presently, this feature is not implemented but the manual realization is shown in Figure 12.

There, the node contact of two grains is converted into a face contact by merging of the surrounding grains and the generated tetrahedrons can satisfy the requirements for their later use. After the clean-up routine the surface information must be exported into a TetGen supported format. Besides the 3D formats "vrml" and "obj" also the export of the TetGen format "poly" is currently implemented.

14 Future Work.

For a better approximation of sandstones a cementation as well as a compaction of the grains has to be implemented. By means of these two additions we can produce the diagenesis process. Furthermore an integration of more trajectories can improve the resulting geometry. To use the generated sediment structure for a numerical simulation, we have to automate the preprocessing conversion of the surface structure into a real 3D-structure.

Besides these "Settle3D" features also a calculation of hydraulic parameters such as permeability, tortuosity, etc. and of mechanical parameters such as bulk modulus, Poisson's ratio, etc. in dependency of the microstructure are future key tasks. In contrast to a continuum approach, modeling of petrophysical properties of sedimentary rocks can directly be linked to a discrete microstructure.

15 Conclusions.

It is possible to generate a simplified sediment structure by rebuilding the sedimentary processes satisfying the fundamental physical laws of sedimentation. The implemented trajectories of the grains (translation, rotation and sliding) are sufficient to describe the natural sedimentation process. The generated structure is similar to a real clastic grainpack and can be converted into a tetrahedron mesh for a later coupled flow simulation.

References

Adams, A. E., MacKenzie, W. S., and Guilford, C., 1986. Atlas der Sedimentgesteine in Dünnschliffen (Atlas of Sedimentary Rocks under the Microscope), Ferdinand Enke Verlag, Stuttgart, Germany, 103pp.

Adler, P. M., 1988. Fractal porous media III: Transversal stokes flow through random and Sierpinski carpets. Transport in Porous Media 3(2), 185–198. doi:10.1007/BF00820345.

Adler, P. M., Jacquin, C. G., and Thovert, J., 1992. The formation factor of reconstructed porous media. Water Resources Research 28(6), 1571–1576. doi:10.1029/92WR00059.

Adler, P. M., Thovert, J.-F., Bekri, S., and Yousefian, F., 2002. Real porous media: Local geometry and transports. Journal of Engineering Mechanics 128(8), 829–839. doi:10.1061/(ASCE)0733-9399(2002)128:8(829).

Bachmat, Y. and Bear, J., 1986. Macroscopic modelling of transport phenomena in porous media. 1: The continuum approach. Transport in Porous Media 1(3), 213–240. doi:10.1007/BF00238181.

Balhoff, M. T., Thompson, K. E., and Hjortsø, M., 2007. Coupling pore-scale networks to continuum-scale models of porous media. Computers & Geosciences 33(3), 393–410. doi:10.1016/j.cageo.2006.05.012.

Bear, J., 1972. Dynamics of Fluids in Porous Media, Dover Publications, Mineola, NY, 784pp.

Buckingham, M. J., 2001. Precision correlations between the geoacoustic parameters of an unconsolidated, sandy marine sediment. Journal of Computational Acoustics 9(1), 101–123. doi:10.1142/S0218396X01000437.

Davis, S. N. and Wiest, R. J. D., 1966. Hydrogeology, John Wiley & Sons Inc., New York, NY, 464pp.

Dobkins, J. E. and Folk, R. L., 1970. Shape development of Tahiti-Nui. Journal of Sedimentary Research 40(4), 1167–1203.

Füchtbauer, H., 1988. Sedimente und Sedimentgesteine (Sediments and Sedimentary Rocks), Schweizerbart'sche Verlagsbuchhandlung, Stuttgart, Germany, 1141pp.

Guéguen, Y., Chelidze, T., and Ravalec, M., 1998. Microstructures, percolation thresholds, and rock physical properties. Tectonophysics 279(1), 23–35. doi:10.1016/S0040-1951(97)00132-7.

Lang, U., 1995. Simulation regionaler Strömungs- und Transportvorgänge in Karstaquiferen mit Hilfe des Doppelkontinuum-Ansatzes: Methodenentwicklung und Parameteridentifikation (Simulation of regional flow and transport in Karst aquifers by means of the double continuum approach: Method development and parameter identification). PhD Dissertation, Institut für Wasserbau, Stuttgart, Germany, 85pp.

Manwart, C., Torquato, S., and Hilfer, R., 2000. Stochastic reconstruction of sandstones. Physical Review E 62, 893–899. doi:10.1103/PhysRevE.62.893.

Matthews, G., Ridgway, C., and Small, J., 1996. Modelling of simulated clay precipitation within reservoir sandstones. Marine and Petroleum Geology

13(5), 581–589. doi:10.1016/0264-8172(95)00099-2.

Mezger, J., Kimmerle, S., and Etzmuß, O., 2002. Improved collision detection and response techniques for cloth animation. Universität Tübingen, Tübingen, Germany, 14pp.

Möller, T., 1997. A fast triangle-triangle intersection test. Journal of Graphics Tools 2(2), 25–30.

Polubarinova-Kocina, P. J., 1962. Theory of Ground Water Movement, Princeton University Press, Princeton, NJ, 636pp.

Reineck, H. E. and Singh, I. B., 1980. Depositional Sedimentary Environments. With Reference to Terrigenous Clastics, 2nd edn., Springer-Verlag, Berlin - Heidelberg - New York, 570pp.

Scholle, P. A., 1979. A Color Illustrated Guide to Carbonate Rock Constituents, Textures, Cements, and Porosities - Memoir 27, 1st edn., The American Association of Petroleum Geologists, Tulsa, Oklahoma, USA, 241pp.

Schopper, J., 1982. Landolt-Börnstein: Physical Properties of Rocks, Springer-Verlag, Berlin - Heidelberg - New York, 373pp.

Selley, R. C., 2000. Applied Sedimentology, 2nd edn., Academic Press, San Diego, California, USA, 523pp.

Spangenberg, E., 2005. Ein fraktales Modellkonzept zur Berechnung physikalischer Gesteinseigenschaften und dessen Anwendung auf die elastischen Eigenschaften poröser Gesteine (A fractal model for physical properties of porous rock: theoretical formulations and application to elastic properties). PhD Dissertation, Geoforschungszentrum Potsdam, Potsdam, Germany, 189pp.

Thovert, J.-F., Yousefian, F., Spanne, P., Jacquin, C. G., and Adler, P. M., 2001. Grain reconstruction of porous media: Application to a low-porosity fontainebleau sandstone. Physical Review E 63,307-323. doi:10.1103/PhysRevE.63.061307.

Trask, P. D., 1932. Origin and Environment of Source Sediments of Petroleum, Gulf Publications, Houston, 323pp.

Trautwein, U., 2005. Poroelastische Verformung und petrophysikalische Eigenschaften von Rotliegend Sandsteinen (Poroelastic deformation and petrophysical properties of Rotliegend Sandstones). PhD Dissertation, Technical University Berlin, Berlin, Germany, 141pp.

Tucker, M. E., 1991. Sedimentary Petrology: An Introduction to the Origin of Sedimentary Rocks, 2nd edn., Blackwell Scientific Publications, Oxford, 262pp.

Underwood, E. E., 1970. Quantitative Stereology, Addison-Wesley Publishing Co., Reading, Massachusetts, 274 pp.

Valvatne, P. H. and Blunt, M. J., 2004. Predictive pore-scale modeling of two-phase flow in mixed wet media. Water Resources Research 40(7), 1–21. doi:10.1029-2003wroo2627.

Wu, Y.-S., Liu, H. H., Bodvarsson, G. S., and Zellmer, K. E., 2001. A triple-continuum approach for modeling flow and transport processes

570   in fractured rock.   Journal of Contaminant Hydrology 73, 145–179.
571   doi:10.1016/j.jconhyd.2004.01.002.

18

A   Appendix

(All of the following calculations refer to Figure 7 on page 34)

A.1   Point-triangle-intersection via translation.

We start with the calculation of the vertical distance (y-direction) between node $\vec{m}$ and triangle T described by the three nodes $\vec{n_0}$, $\vec{n_1}$, and $\vec{n_2}$. The edges $\vec{n_{10}}=\vec{n_1}\text{-}\vec{n_0}$ and $\vec{n_{20}}=\vec{n_2}\text{-}\vec{n_0}$ of the triangle T span the plane P, with

$$P : \vec{n_0} + s \times \vec{n_{10}} + t \times \vec{n_{20}}. \tag{A.1}$$

The vertical projection of $\vec{m}$ into the plane P leads to the image

$$\vec{m}' = \vec{n_0} + s \times \vec{n_{10}} + t \times \vec{n_{20}} \tag{A.2}$$

with the same x, z coordinates as $\vec{m}$. Therefore, the equations

$$m'_x = m_x = n_{0x} + s \times n_{10x} + t \times n_{20x}, \tag{A.3}$$

$$m'_z = m_z = n_{0z} + s \times n_{10z} + t \times n_{20z} \tag{A.4}$$

lead to

$$s = \frac{n_{20x} \times (m_z - n_{0z}) - n_{20z} \times (m_x - n_{0x})}{n_{20x} \times n_{10z} - n_{20z} \times n_{10x}}, \tag{A.5}$$

$$t = \frac{n_{10x} \times (m_z - n_{0z}) - n_{10z} \times (m_x - n_{0x})}{n_{10x} \times n_{20z} - n_{10z} \times n_{20x}}. \tag{A.6}$$

The image m' is inside the triangle area if, $(0 \leq s \leq 1)$, $(0 \leq t \leq 1)$ and $(s + t \leq 1)$. Under these circumstances, the y-value of the image can be calculated

$$m'_y = n_{0y} + s \times n_{10y} + t \times n_{20y}, \tag{A.7}$$

and the vertical distance d between m and T is

$$d = |m'_y - m_y|. \tag{A.8}$$

19

A.2 Line-line-intersection via translation.

Two lines (L_1, L_2) in three dimensional space are given by the nodes $\vec{m_0}$, $\vec{m_1}$ and $\vec{n_0}$, $\vec{n_1}$, respectively. By means of the direction vectors $\vec{m_{10}}=\vec{m_1}-\vec{m_0}$ and $\vec{n_{10}}=\vec{n_1}-\vec{n_0}$, the linear equations are given by:

$$L_1 : \vec{m_0} + s \times \vec{m_{10}}, \tag{A.9}$$

$$L_2 : \vec{n_0} + t \times \vec{n_{10}}. \tag{A.10}$$

The vertical distance of both lines is the shortest vertical distance between one point $\vec{m}$ at line L_1 and its projection point $\vec{m}'$ at line L_2. Both points must have the same x and z coordinates. Therefore,

$$\vec{m} = \vec{m_0} + s \times \vec{m_{10}}, \tag{A.11}$$

$$\vec{m}' = \vec{n_0} + t \times \vec{n_{10}} \tag{A.12}$$

and

$$m'_x = m_x, \tag{A.13}$$

$$m'_z = m_z \tag{A.14}$$

lead to:

$$m_{0x} + s \times m_{10x} = n_{0x} + t \times n_{10x}, \tag{A.15}$$

$$m_{0z} + s \times m_{10z} = n_{0z} + t \times n_{10z} \tag{A.16}$$

where s and t can be calculated as:

$$s = \frac{n_{10z} \times (m_{0x} - n_{0x}) - n_{10x} \times (m_{0z} - n_{0z})}{m_{10z} \times n_{10x} - m_{10x} \times n_{10z}}, \tag{A.17}$$

$$t = \frac{m_{10z} \times (n_{0x} - m_{0x}) - m_{10x} \times (n_{0z} - m_{0z})}{n_{10z} \times m_{10x} - n_{10x} \times m_{10z}}. \tag{A.18}$$

Under the assumptions that $\vec{m}$ is part of line section $\overline{m_0 m_1}$ ($0 \leq s \leq 1$) and $\vec{n}$ is part of line section $\overline{n_0 n_1}$ ($0 \leq t \leq 1$), the y-values of both points can be calculated:

$$m_y = m_{0y} + s \times m_{10y}, \tag{A.19}$$

$$m'_y = n_{0y} + t \times n_{10y} \tag{A.20}$$

and the vertical distance d between the lines is:

$$d = |m'_y - m_y|. \tag{A.21}$$

A.3 Point-triangle-intersection via rotation.

We assume, that one point $\vec{m}$ will hit a triangle T described by the three nodes $\vec{n_0}$, $\vec{n_1}$, and $\vec{n_2}$ via a rotation around the z axis. The two direction vectors $\vec{n_{10}} = \vec{n_1} - \vec{n_0}$ and $\vec{n_{20}} = \vec{n_2} - \vec{n_0}$ of the triangle T span a plane P, with

$$P : \vec{n_0} + s \times \vec{n_{10}} + t \times \vec{n_{20}}. \tag{A.22}$$

The resulting image point $\vec{m}'$ must be in the same x,y plane as $\vec{m}$. Furthermore, the image must be located inside P, more precisely inside T, and must have the same distance from the z-axis as $\vec{m}$. Therefore, the following equations must be satisfied:

$$\vec{m}' = \vec{n_0} + s \times \vec{n_{10}} + t \times \vec{n_{20}}, \tag{A.23}$$

$$\begin{pmatrix} m'_x \\ m'_y \\ m'_z \end{pmatrix} = \begin{pmatrix} n_{0x} \\ n_{0y} \\ n_{0z} \end{pmatrix} + s \times \begin{pmatrix} n_{10x} \\ n_{10y} \\ n_{10z} \end{pmatrix} + t \times \begin{pmatrix} n_{20x} \\ n_{20y} \\ n_{20z} \end{pmatrix}, \tag{A.24}$$

$$m_z = m'_z, \tag{A.25}$$

$$m_x^2 + m_y^2 = m_x'^2 + m_y'^2. \tag{A.26}$$

By means of equation (A.25) the control variable t can be expressed in terms of s:

$$t = \frac{m_z - n_{0z} - s \times n_{10z}}{n_{20z}}. \tag{A.27}$$

and with equation (A.24)

$$m'_x = n_{0x} + s \times n_{10x} + \frac{m_z - n_{0z} - s \times n_{10z}}{n_{20z}} \times n_{20x}, \tag{A.28}$$

$$m'_y = n_{0y} + s \times n_{10y} + \frac{m_z - n_{0z} - s \times n_{10z}}{n_{20z}} \times n_{20y} \tag{A.29}$$

21

can be calculated. After expansion we receive:

$$m'_x = \frac{1}{n_{20z}}[s \times (n_{10x} \times n_{20z} - n_{10z} \times n_{20x})$$
$$+n_{0x} \times n_{20z} + (m_z - n_{0z}) \times n_{20x}], \tag{A.30}$$

$$m'_y = \frac{1}{n_{20z}}[s \times (n_{10y} \times n_{20z} - n_{10z} \times n_{20y})$$
$$+n_{0y} \times n_{20z} + (m_z - n_{0z}) \times n_{20x}]. \tag{A.31}$$

With the substitutions:

$$X_1 = n_{10x} \times n_{20z} - n_{10z} \times n_{20x}, \tag{A.32}$$

$$X_2 = n_{0x} \times n_{20z} + (m_z - n_{0z}) \times n_{20x}, \tag{A.33}$$

$$Y_1 = n_{10y} \times n_{20z} - n_{10z} \times n_{20y}, \tag{A.34}$$

$$Y_2 = n_{0y} \times n_{20z} + (m_z - n_{0z}) \times n_{20y}, \tag{A.35}$$

we can simplify (A.30) and (A.31) to:

$$m'_x = \frac{s \times X_1 + X_2}{n_{20z}}, \tag{A.36}$$

$$m'_y = \frac{s \times Y_1 + Y_2}{n_{20z}}. \tag{A.37}$$

The insertion of (A.36) and (A.37) into (A.26) leads to:

$$(m_x^2 + m_y^2) \times n_{20z}^2 = (s \times X_1 + X_2)^2 + (s \times Y_1 + Y_2)^2. \tag{A.38}$$

With the further substitution $Z = (m_x^2 + m_y^2) \times n_{20z}^2$ we can build the quadratic equation:

$$s^2 \times (X_1^2 + Y_1^2) + 2s \times (X_1 X_2 + Y_1 Y_2) + X_2^2 + Y_2^2 - Z = 0. \tag{A.39}$$

With $A = X_1^2 + Y_1^2$, $B = X_1 X_2 + Y_1 Y_2$ and $C = X_2^2 + Y_2^2 - Z$, we can solve the quadratic equation:

$$s^2 \times A + 2s \times B + C = 0. \tag{A.40}$$

which results in:

$$s_{1,2} = -\frac{B}{A} \pm \frac{\sqrt{B^2 - AC}}{A}. \tag{A.41}$$

By means of (A.27) the associated $t_{1,2}$ can be calculated. The image m' is inside the triangle area if one of the $s_{1,2}$ and its associated $t_{1,2}$ satisfy the following conditions, $(0 \leq s \leq 1)$, $(0 \leq t \leq 1)$ and $(s + t \leq 1)$. Under these conditions the x,y-value of the image can be calculated

$$m'_x = n_{0x} + s \times n_{10x} + t \times n_{20x}, \tag{A.42}$$

$$m'_y = n_{0y} + s \times n_{10y} + t \times n_{20y}, \tag{A.43}$$

and the angle which rotates $\vec{m}$ into $\vec{m}'$ can be determined by means of these coordinates.

A.4 Line-line-intersection via rotation.

The line L_1 given by the nodes m_0 and m_1 is rotated around the z-axis and can possibly collide with line L_2 given by the nodes n_0 and n_1. Four different cases can then occur: No collision of both lines, touching in one osculation point, intersection in up to two points and an infinite amount of collision points if the lines are parallel and have the same distance to the z-axis. In the intersection case one point m at line L_1 will hit one point m' at line L_2 with the included angle α. The linear equations with the two direction vectors $\vec{m_{10}} = \vec{m_1} - \vec{m_0}$ and $\vec{n_{10}} = \vec{n_1} - \vec{n_0}$ for the lines are:

$$L_1 : \vec{m_0} + s \times \vec{m_{10}}, \tag{A.44}$$

$$L_2 : \vec{n_0} + t \times \vec{n_{10}}. \tag{A.45}$$

We assume that the resulting image point $\vec{m}'$ must be in the same x,y plane as $\vec{m}$. Furthermore, the image must satisfy the linear equation L_2, $\vec{m}$ must be at line L_1 and both points must have the same distance from the z-axis. Therefore, the following equations must be fulfilled:

$$\vec{m} = \vec{m_0} + s \times \vec{m_{10}}, \tag{A.46}$$

$$\begin{pmatrix} m_x \\ m_y \\ m_z \end{pmatrix} = \begin{pmatrix} m_{0x} \\ m_{0y} \\ m_{0z} \end{pmatrix} + s \times \begin{pmatrix} m_{10x} \\ m_{10y} \\ m_{10z} \end{pmatrix} \tag{A.47}$$

23

and

$$\vec{m'} = \vec{n_0} + t \times \vec{n_{10}}, \tag{A.48}$$

$$\begin{pmatrix} m'_x \\ m'_y \\ m'_z \end{pmatrix} = \begin{pmatrix} n_{0x} \\ n_{0y} \\ n_{0z} \end{pmatrix} + t \times \begin{pmatrix} n_{10x} \\ n_{10y} \\ n_{10z} \end{pmatrix}, \tag{A.49}$$

$$m_z = m'_z, \tag{A.50}$$

$$m_x^2 + m_y^2 = m_x'^2 + m_y'^2. \tag{A.51}$$

By means of (A.50) the control variable t can be expressed in terms of s:

$$t = \frac{m_{0z} - n_{0z} + s \times m_{10z}}{n_{10z}}. \tag{A.52}$$

The insertion of (A.52) into (A.49) leads to the x,y components of m':

$$m'_x = n_{0x} + \frac{m_{0z} - n_{0z} + s \times m_{10z}}{n_{10z}} \times n_{10x}, \tag{A.53}$$

$$m'_y = n_{0y} + \frac{m_{0z} - n_{0z} + s \times m_{10z}}{n_{10z}} \times n_{10y}. \tag{A.54}$$

After expansion the equations (A.53) and (A.54) can be rewritten as:

$$m'_x = \frac{n_{0x} \times n_{10z} + (m_{0z} - n_{0z}) \times n_{10x} + s \times m_{10z} \times n_{10x}}{n_{10z}}, \tag{A.55}$$

$$m'_y = \frac{n_{0y} \times n_{10z} + (m_{0z} - n_{0z}) \times n_{10y} + s \times m_{10z} \times n_{10y}}{n_{10z}}. \tag{A.56}$$

With the following substitutions

$$X_1 = m_{10z} \times n_{10x}, \tag{A.57}$$

$$X_2 = n_{0x} \times n_{10z} + (m_{0z} - n_{0z}) \times n_{10x}, \tag{A.58}$$

$$Y_1 = m_{10z} \times n_{10y}, \tag{A.59}$$

$$Y_2 = n_{0y} \times n_{10z} + (m_{0z} - n_{0z}) \times n_{10y}, \tag{A.60}$$

24

they reduce to:

$$m'_x = \frac{s \times X_1 + X_2}{n_{10z}}, \tag{A.61}$$

$$m'_y = \frac{s \times Y_1 + Y_2}{n_{10z}}. \tag{A.62}$$

The combination of the reduced equations and (A.51) results in:

$$(s \times X_1 + X_2)^2 + (s \times Y_1 + Y_2)^2$$
$$= [(m_x + s \times m_{10x})^2 + (m_y + s \times m_{10y})^2] \times n_{10z}^2, \tag{A.63}$$

which can be converted into a quadratic equation:

$$s^2 \times [X_1^2 + Y_1^2 - (m_{10x}^2 + m_{10y}^2) \times n_{10z}^2]$$
$$+2s \times [X_1 X_2 + Y_1 Y_2 - (m_{0x} m_{10x} - m_{0y} m_{10y}) \times n_{10z}^2]$$
$$+[X_2^2 + Y_2^2 - (m_{0x}^2 + m_{0y}^2) \times n_{10z}^2 = 0]. \tag{A.64}$$

Replacing the coefficients of the quadratic equation by A, B and C leads to the simpler expression:

$$s^2 \times A + 2s \times B + C = 0, \tag{A.65}$$

which results in:

$$s_{1,2} = -\frac{B}{A} \pm \frac{\sqrt{B^2 - AC}}{A}. \tag{A.66}$$

By means of (A.52) the associated $t_{1,2}$ can be calculated. Under the conditions $(0 \leq s \leq 1)$ and $(0 \leq t \leq 1)$, the point m and its image m' are located at their specific line sections and can be calculated by using (A.47) and (A.49). By means of these coordinates the angle α can be explicitly determined.

B Appendix

Calculating the 2D and 3D porosity of a sphere with radius a inside a cube with side length $2a$. The volume of the cube is:

$$V_{cube} = (2a)^3 = 8a^3, \tag{B.1}$$

and the volume of the included sphere is:

$$V_{sphere} = \frac{4}{3}\pi a^3. \tag{B.2}$$

Therefore the 3D porosity is:

$$P_{3D} = \frac{V_{cube} - V_{sphere}}{V_{cube}} = \frac{8a^3 - \frac{4}{3}\pi a^3}{8a^3} = 1 - \frac{1}{6}\pi. \tag{B.3}$$

We assume, that the sphere inside the cube is cut into n pieces as shown in Figure 13. There, k is the position of the cut. The radius r of the resulting circle at position k is:

$$r(k) = \sqrt{a^2 - (2a\frac{k}{n} - a)^2}, \tag{B.4}$$

and the area of the resulting circle at position k is:

$$A_{circle}(k) = \pi r(k)^2 = \pi(a^2 - (2a\frac{k}{n} - a)^2). \tag{B.5}$$

The area of the square including the circle is:

$$A_{square} = (2a)^2 = 4a^2 = const., \tag{B.6}$$

and the area of pore space is:

$$A_{pore}(k) = A_{square} - A_{circle}(k) = 4a^2 - \pi(a^2 - (2a\frac{k}{n} - a)^2). \tag{B.7}$$

The statistic porosity of one cross section can be assumed as the mean of all porosities of these cutting planes:

$$P_{2D} = \frac{1}{n}\sum_{k=0}^{n}\frac{A_{pore}(k)}{A_{square}}$$

$$= \frac{1}{4a^2 n}\sum_{k=0}^{n}(4a^2 - \pi a^2 + 4\pi a^2\frac{k^2}{n^2} - 4\pi a^2\frac{k}{n} + \pi a^2)$$

$$= \frac{1}{4a^2 n} \times (4a^2\sum_{k=0}^{n}1 + \frac{4\pi a^2}{n^2}\sum_{k=0}^{n}k^2 - \frac{4\pi a^2}{n}\sum_{k=0}^{n}k)$$

$$= 1 + \frac{\pi}{n^3}\sum_{k=0}^{n}k^2 - \frac{\pi}{n^2}\sum_{k=0}^{n}k$$

26

$$= 1 + \frac{\pi}{n^3} \times \frac{n}{6}(n+1)(2n+1) - \frac{\pi}{n^2} \times \frac{n^2+n}{2}$$

$$= 1 + \frac{\pi}{3} + \frac{\pi}{2n} + \frac{\pi}{6n^2} - \frac{\pi}{2} - \frac{\pi}{2n} \tag{B.8}$$

$$\lim_{n\to\infty} 1 + \frac{\pi}{3} + \frac{\pi}{2n} + \frac{\pi}{6n^2} - \frac{\pi}{2} - \frac{\pi}{2n} = 1 + \frac{\pi}{3} - \frac{\pi}{2} = 1 - \frac{1}{6}\pi. \tag{B.9}$$

(q.e.d.)

List of Tables

List of Figures

29

Table 1

Number of nodes N, edges E and faces F as well as surface area A and volume V at different refinement levels. (*percentage of circumscribed sphere)

	Icosahedron	1st order refinement	2nd order refinement	3rd order refinement
nodes N	12	42	162	642
edges E	30	120	480	1920
faces F	20	80	320	1280
volume V*	60.55%	87.35%	96.62%	99.14%
surface area A*	76.19%	92.83%	98.12%	99.52%
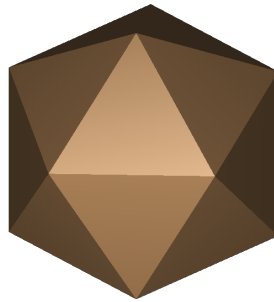
Fig. 1. Regular icosahedron
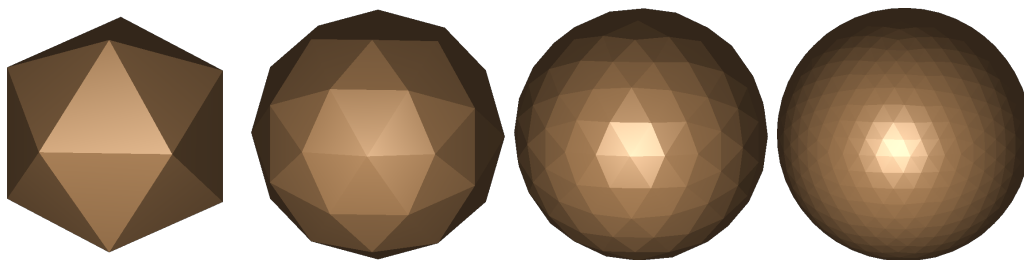
Fig. 2. Refinement of surface by subdivision of existing faces. Starting with an icosahedron (left) and increasing the refinement level stepwise by one (right).

Table 2
Number G, volume $V[mm^3]$, porosity $P_t/P_e[\%]$ and inner surface area $S[mm^2]$ of settled grains for ten simulated sandstones.

		translation	translation rotation	translation rotation sliding
one type 0.2 - 0.63mm	$G:$	195	396	375
	$V:$	6.03	13.06	13.49
	$P_t/P_e:$	77.67/77.54	51.62/51.36	50.05/49.76
	$S:$	85.53	182.62	184.44
one type 0.063 - 0.63mm	$G:$	1803	3203	2957
	$V:$	4.09	14.40	14.35
	$P_t/P_e:$	84.85/84.67	46.68/46.23	46.87/46.42
	$S:$	122.16	295.89	288.51
one type 0.02 - 0.63mm	$G:$		30992	
	$V:$		15.25	
	$P_t/P_e:$		43.53/42.85	
	$S:$		451.52	
two types 0.2 - 0.63mm	$G:$		479	561
	$V:$		10.87	11.97
	$P_t/P_e:$		59.75/59.47	55.65/55.37
	$S:$		183.71	201.15
three types 0.2 - 0.63mm	$G:$			739
	$V:$			10.85
	$P_t/P_e:$			59.80/59.48
	$S:$			223.28

Table 3

Comparison of 2D and 3D porosities by means of x, y and z cutting planes.

Grain			Porosity [%]					Ratio
types	size[mm]	moves	3D	2D	2Dx	2Dy	2Dz	3D/2D
one	0.2-0.63	t	**77.7**	**77.9**	78.4	79.6	75.6	**1.00**
one	0.2-0.63	tr	**51.6**	**49.6**	51.6	49.8	47.4	**1.04**
one	0.2-0.63	trs	**50.1**	**48.8**	47.6	50.5	48.3	**1.03**
one	0.063-0.63	t	**84.9**	**86.7**	84.9	89.5	85.8	**0.98**
one	0.063-0.63	tr	**46.7**	**44.8**	44.1	46.2	44.1	**1.04**
one	0.063-0.63	trs	**46.9**	**43.7**	44.5	47.3	39.2	**1.07**
one	0.02-0.63	tr	**43.5**	**43.4**	42.6	48.8	38.7	**1.00**
two	0.2-0.63	tr	**59.8**	**56.8**	50.8	63.8	55.8	**1.05**
two	0.2-0.63	trs	**55.7**	**58.8**	57.5	62.4	56.4	**0.95**
three	0.2-0.63	tr	**59.8**	**62.1**	62.3	66.4	57.7	**0.96**

	origin	with additional noise	with limiting border
$a_1 = a_2 = a_3$			
$a_1 \neq a_2 \neq a_3$			
$a_1 = a_2 \neq a_3$			
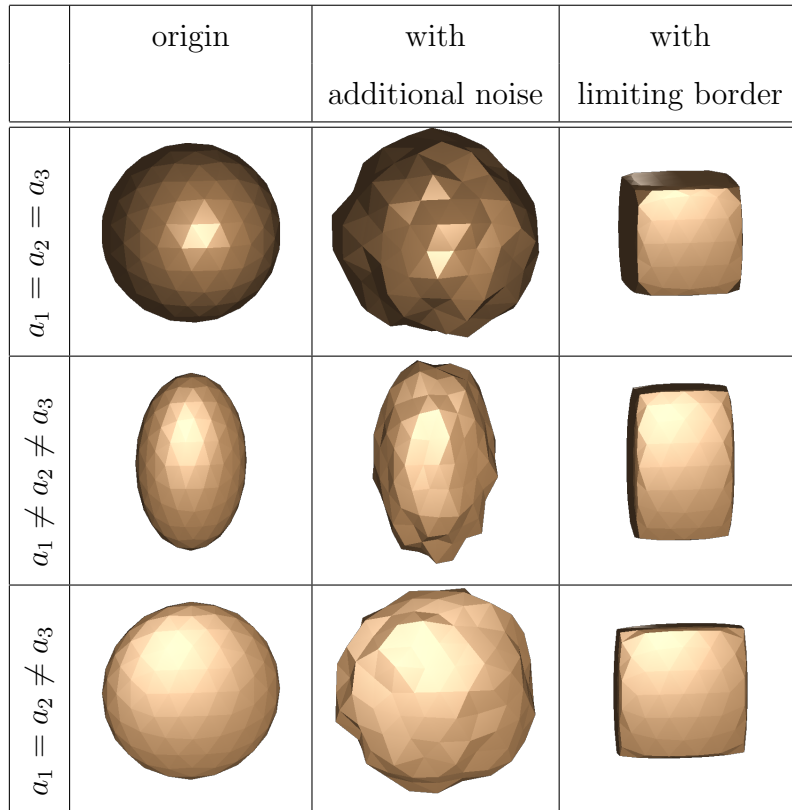
Fig. 3. Nine selected morphology variations of "Settle3D" resulting from different aspect ratios, roughness and limiting borders.
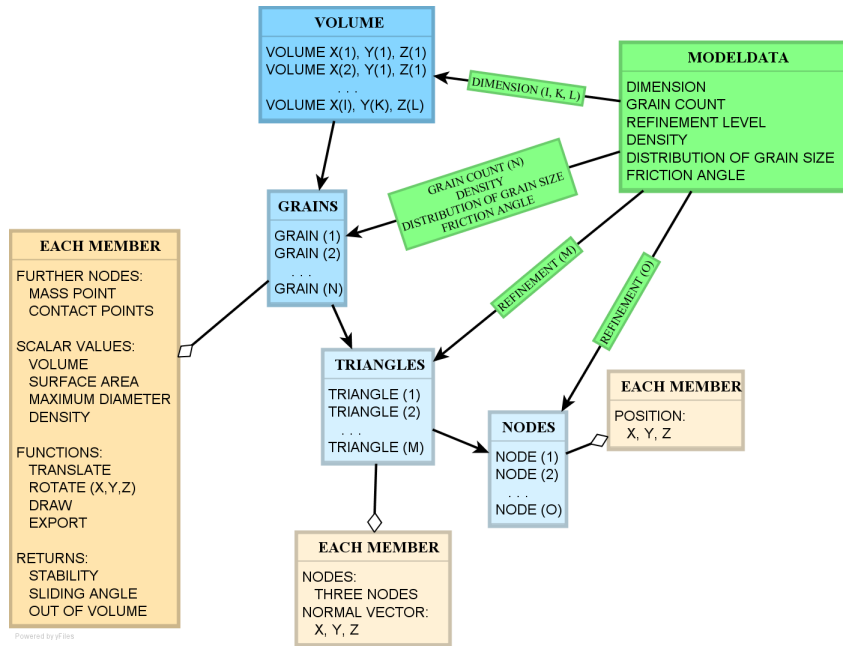
Fig. 4. Structure of sedimentary tool is coarsely classified by geometric data (from single node up to entire volume) as well as its typical attributes and can be modified by parameters which are included in user-defined model-data.
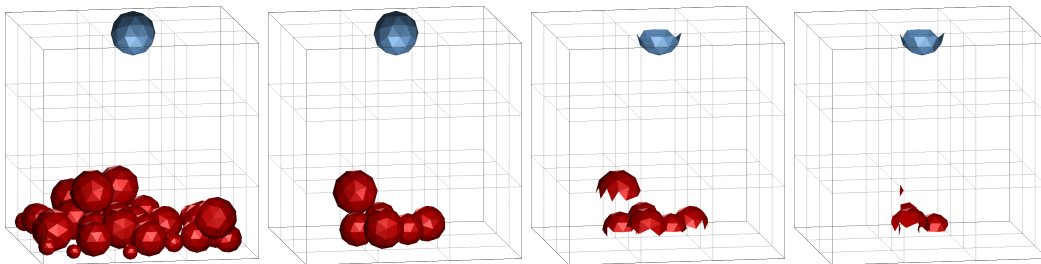
Fig. 5. Preselection of triangles which are used to calculate vertical distance between falling grain and settled grains: using grain size and model data dimension(left), grain-grain dimension, triangle orientation given by normal vectors and triangle–triangle dimension (right).
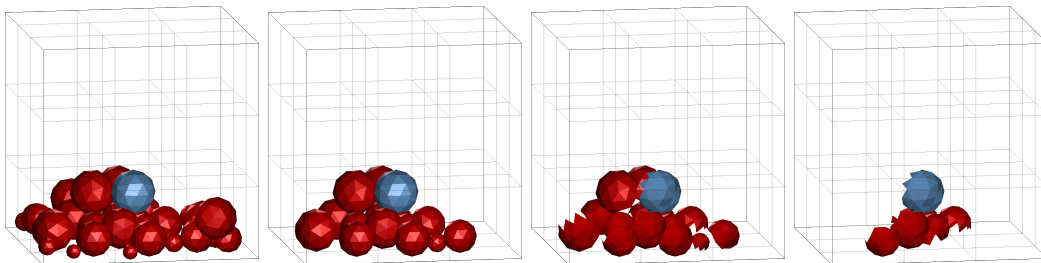
Fig. 6. Preselection of triangles which are selected to calculate rotation process of falling grain: using grain size and model data dimension(left), grain-grain dimension, triangle orientation given by normal vectors and triangle-triangle dimension (right).

33
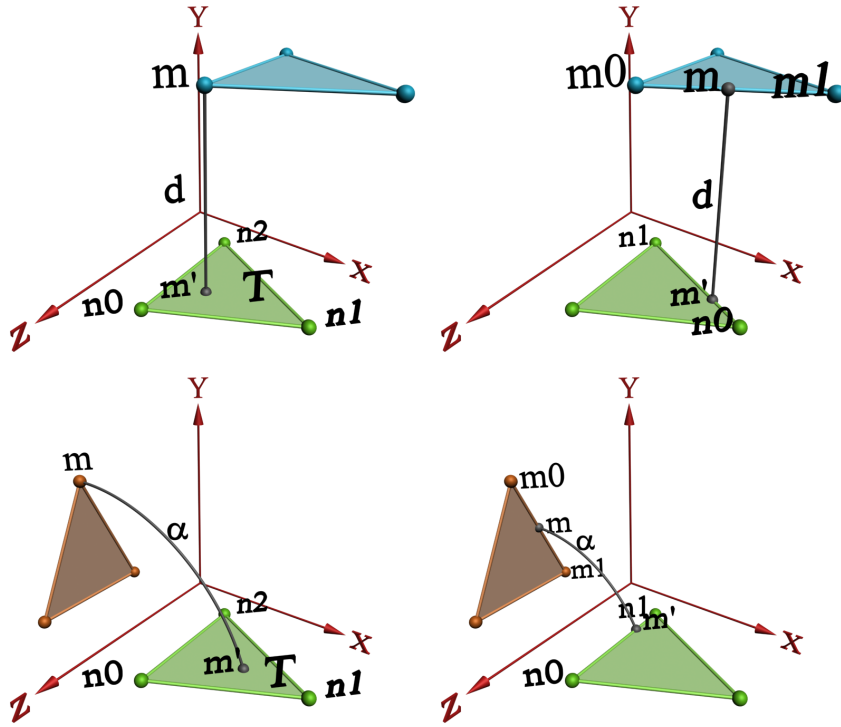
Fig. 7. Calculation of collision point $\overrightarrow{m}'$ and resulting distance d between $\overrightarrow{m}$ and $\overrightarrow{m}'$ caused by vertical translation of $\overrightarrow{m}$ into triangle plane T (top left). Calculation of two collision points $\overrightarrow{m}$ and $\overrightarrow{m}'$ and resulting distance d between $\overrightarrow{m}$ and $\overrightarrow{m}'$ caused by vertical translation of line $\overline{m_0 m_1}$ along y-axis into line $\overline{n_0 n_1}$ (top right). Calculation of collision point $\overrightarrow{m}'$ and included angle α between $\overrightarrow{m}$ and $\overrightarrow{m}'$ caused by rotation of $\overrightarrow{m}$ around z-axis into triangle plane T (bottom left). Calculation of two collision points $\overrightarrow{m}$ and $\overrightarrow{m}'$ and resulting angle α caused by rotation of line $\overline{m_0 m_1}$ around z-axis into line $\overline{n_0 n_1}$ (bottom right).
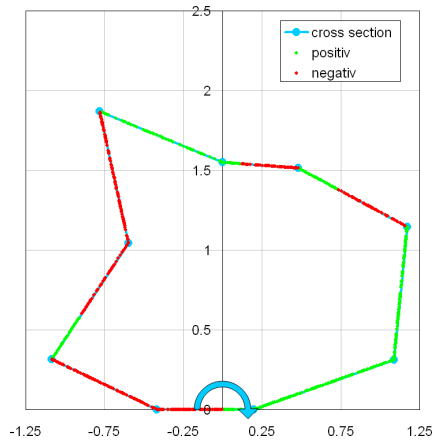
Fig. 8. Cross-section of one single grain including post-selection of calculated intersection points for a positive rotation. Sub-lines rotating away from grain can collide with other grains (green); sub-lines in shadow of rotating nodes can not collide (red).

34
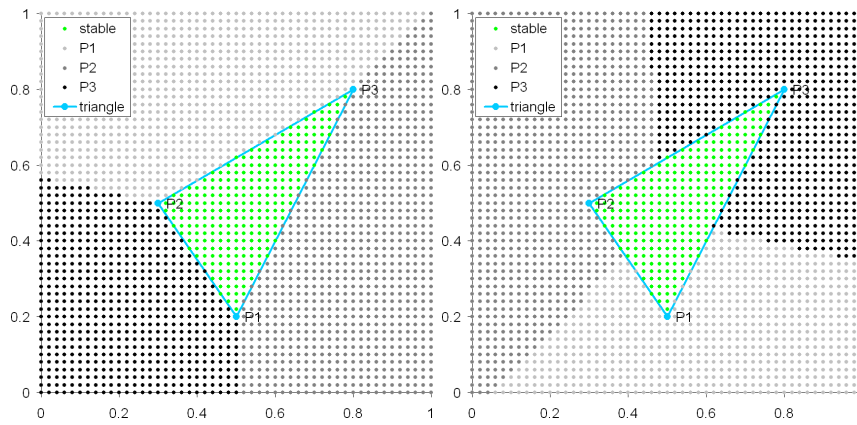
Fig. 9. Stability check for a falling grain with three existing contact points (P1, P2 and P3). Dots are possible positions of a vertical projection from CG. Color index shows, which contact points will lose contact for next rotation step depending on CG location. CG is located above contact point plane (left) and below (right).
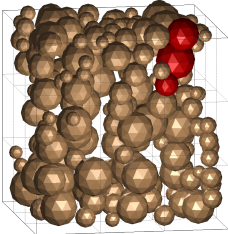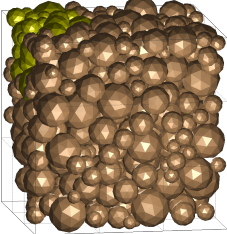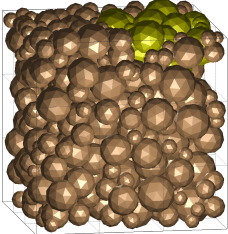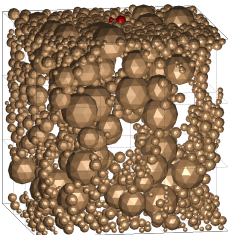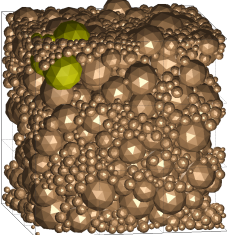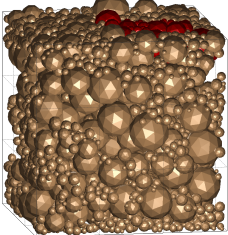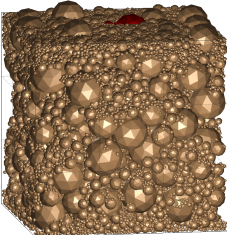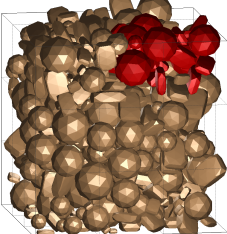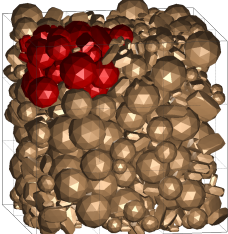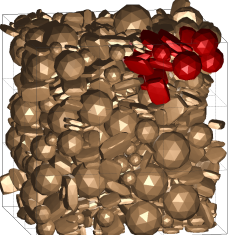
	translation	translation rotation	translation rotation sliding
one type 0.2 - 0.63mm			
one type 0.063 - 0.63mm			
one type 0.02 - 0.63mm			
two types 0.2 - 0.63mm			
three types 0.2 - 0.63mm			

Fig. 10. Ten different models of sandstone. Boundary conditions vary in grain size, amount of grain types and in combination of sedimentary processes. For all models volume as well as detail level were same.
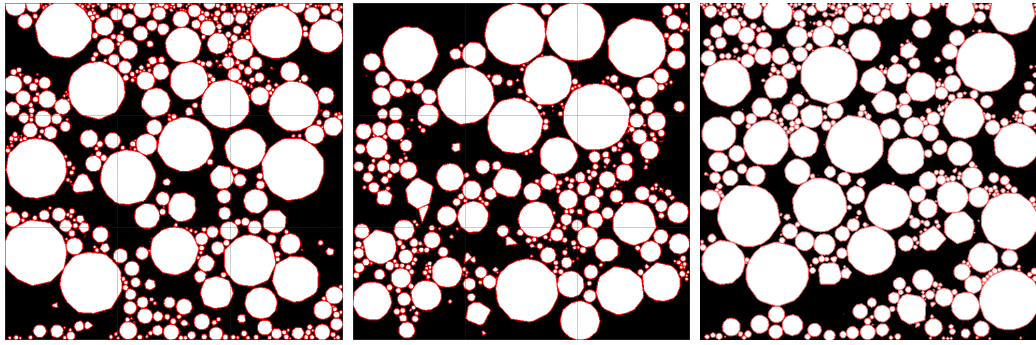
Fig. 11. Cross section images of quartz model including three grain fractions taken at 50% of x (left), y (middle) and z (right) axis.
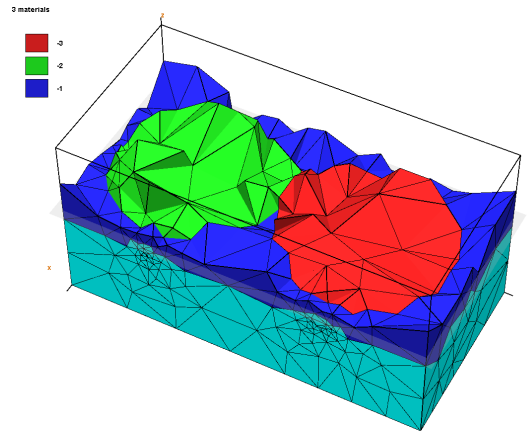

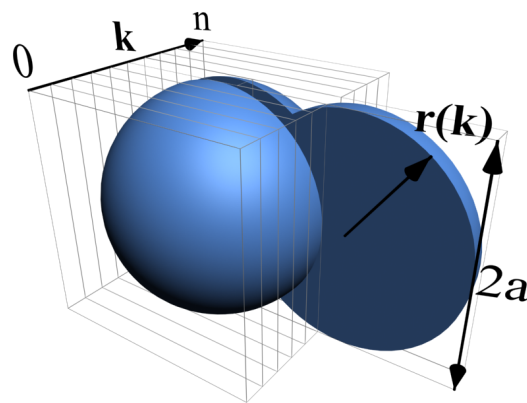Fig. 12. Resulting tetrahedron mesh of two manually connected grains.

Fig. 13. Schematic representation of a dissected sphere